Corrosion Science 194 (2022) 109925

Contents lists available at ScienceDirect

Corrosion Science

journal homepage: www.elsevier.com/locate/corsci

The effect of laser shock peening with and without protective coating on intergranular corrosion of sensitized AA5083

Jan Kaufman [a,b,*], Jan Racek [a], Miroslav Cieslar [c], Peter Minárik [c], Matthew A. Steiner [d], Seetha R. Mannava [d], Vijay K. Vasudevan [e], Anurag Sharma [d], Marek Böhm [a,b], Jan Brajer [a], Jan Pilař [a], Ladislav Pína [b], Tomáš Mocek [a]

[a] HiLASE Centre, Institute of Physics of the Czech Academy of Sciences, Czech Republic
[b] Czech Technical University in Prague, Faculty of Nuclear Sciences and Physical Engineering, Czech Republic
[c] Charles University, Faculty of Mathematics and Physics, Czech Republic
[d] University of Cincinnati, Mechanical and Materials Engineering Department, Cincinnati, OH, United States
[e] University of North Texas, Department of Materials Science and Engineering, Denton, TX, United States

ARTICLE INFO

Keywords:
A. aluminum
A. magnesium
B. cyclic voltammetry
B. polarization
C. intergranular corrosion
C. passivity

ABSTRACT

Laser Shock Peening with (LSP) and without protective coating (LPwC) was applied to sensitized AA5083 followed by electrochemical analysis. Potentiodynamic tests indicated a region of increased passivity for the LPwC samples with lower corrosion current. Similarly, significantly reduced intergranular corrosion rate was observed during potentiostatic polarization after LPwC treatment while LSP samples showed only a negligible improvement. The results are attributed to the unique recast surface layer composed of a modified oxide film followed by an embedded oxygen-rich aluminum nanoparticles sub-surface layer without grain boundary β-phase created during laser pulse interaction with the surface when no coating was applied.

1. Introduction

5xxx series Mg rich aluminum alloys are high strength-to-weight ratio weldeable materials with excellent general corrosion resistance. As such, the 5xxx series found its natural domain in marine industry, both commercial and military, where it allows for construction of lighter, faster and more fuel efficient ships. Despite their good initial corrosion resistance, it has been established that alloys containing more than 3.5% of Mg can become sensitized when exposed to elevated temperature (as low as 50 °C) for prolonged periods of time [1].

Initially, the magnesium atoms exist in the form of a metastable solid solution (α-phase) distributed uniformly across the aluminum matrix. When the material is exposed to moderately elevated temperatures, the Mg atoms diffuse from the matrix to low energy sites such as the grain boundaries [2,3]. Eventually, β-phase precipitates (Mg_2Al_3) are formed at grain boundaries and the matrix becomes electrochemically heterogeneous. According to Birbilis et al. [4], the breakdown potential E_b of the bulk β-phase is -0.95 V_{SCE} which is lower than -0.78 V_{SCE} of the sensitized alloy. In the near neutral salt solutions of sea water, the grain boundary acts as an anode to the adjacent magnesium depleted cathodic regions, causing selective dissolution of the anodic precipitates. In a sensitized material, increasing β-phase coverage [5,6] eventually leads to corrosion spreading to neighboring precipitates resulting in a continuous network of corroded grain boundaries and intergranular corrosion (IGC). Although IGC is primarily driven by chemical forces and no stresses are required for the corroded network to develop, the presence of tensile stresses can lead to intergranular stress corrosion cracking (IGSCC), often resulting in a critical failure and subsequent costly repairs. Golumbfskie et al. [7] report, for instance, that the trend of average number of stress corrosion cracks discovered per ship inspection has been steadily rising since 1990 where it was more than triple the amount in 2015.

In order to combat IGC and IGSCC in AA5083, several approaches can be adopted. Searles et al. [8] opted for the anodic protection route where, using lower electric potential, the material is brought to its passive region where it forms a natural protective oxide layer. They found that samples polarized below the β-phase E_b showed almost no evidence of IGSCC. Seong et al. [9,10] studied the effect of chromate, silicate, or vanadate ions based chemical additives as corrosion inhibitors. They showed that the addition of K_2CrO_4 and $NaVO_3$ into the

* Correspondence to: HiLASE Centre, Institute of Physics of the Czech Academy of Sciences, Za Radnici 828, 252 41 Dolni Brezany, Czech Republic.
E-mail address: jan.kaufman@hilase.cz (J. Kaufman).

https://doi.org/10.1016/j.corsci.2021.109925
Received 11 May 2021; Received in revised form 21 October 2021; Accepted 28 October 2021
Available online 1 November 2021
0010-938X/© 2021 The Author(s). Published by Elsevier Ltd. This is an open access article under the CC BY license (http://creativecommons.org/licenses/by/4.0/).

3.5 wt% NaCl environment resulted in strain curves essentially equal to those in air. The mechanism of inhibition in this case was mainly through the inhibition of cathodic reaction rather than the anodic dissolution. Both of these approaches, however, are not suited for sea environment.

It has been established that SCC behavior of various metallic alloys can also be influenced by Laser Shock Peening (LSP) via tensile stress removal [11–14]. In typical LSP setup, a protective overlay or coating in the form of vinyl or aluminum tape is used to protect the sample surface from heat effects that occur during laser absorption. LSP without protective coating (LPwC) usually causes partial surface melting which in turn creates tensile stresses on the surface that can act as crack initiation sites. However, Sano et al. [15,16] demonstrated that by applying low pulse energies and high pulse densities in aqueous environment, the tensile stresses can be converted to compressive and LPwC can still be beneficial when it comes to improving fatigue performance and SCC. Furthermore, studies conducted both with [17,18] and without protective coating [19,20] indicate that LSP does have a positive effect on corrosion behavior of aluminum alloys which is usually indicated by lower corrosion current density and increase in E_b. The main corrosion mechanism in these studies, however, is pitting. Very little to no investigation has been carried out when it comes to the influence of LSP on IGC. In this work, we focus on investigating both LSP and LPwC setups, in order to find what difference the presence or absence of a protective coating makes in terms of corrosion resistance of AA5083 and IGC behavior specifically.

2. Experimental

2.1. Material

A commercial aluminum alloy 5083-H116 in a form of 18" × 12" × 0.25" plate was used in this study. The chemical composition is shown in Table 1. A part of the plate was sectioned off using electric discharge machine to serve as a control group (as received) for the sensitized condition. The rest of the original plate was sensitized at 100 °C for 60 days and air cooled upon removal. Both sensitized and as received plates were then sectioned into 40 mm × 40 mm × 6.35 mm square coupons and polished to 1200 grit with silicon carbide paper followed by 1 μm mirror polish using diamond suspensions. After deionized (DI) water rinsing, the samples were ultrasonically cleaned in ethanol (C_2H_5OH) for 30 s followed by an air drying.

The IGC susceptibility of samples was assessed using the Nitric Acid Mass Loss Test (NAMLT) as determined by the ASTM G67 standard [21]. The Degree of Sensitization (DoS) was determined to be 5 mg/cm^2 and 44.6 mg/cm^2 for the as received (AR) and sensitized (SE) material, respectively, which puts the sensitized samples into the IGC susceptible category.

2.2. Laser treatment

During Laser Shock Peening, a laser pulse with an energy of several Joules is focused onto a specimen surface that has typically been covered with a thin protective layer and topped with a thin (~1 mm) water layer. As the laser pulse is absorbed, a strong shock wave with a magnitude of several GPa [22] is generated, enhanced by the water confinement. The shock wave propagates through the material, creating plastic strain and generating compressive residual stresses (Fig. 1a). With the protective layer absent, the plasma is created directly on top of the irradiated surface and leads to its partial melting. Treatment of larger areas is achieved via placing laser shots next to each other in a predetermined peening pattern.

In this case, both the LSP and LPwC treatments were carried out using first power pre-amplifier of Yb:YAG laser system Bivoj operating at 1030 nm with 10 Hz repetition rate [23]. For some cases the light from Bivoj was converted to 515 nm using non-linear conversion. In all cases, the 14 ns long pulses had rectangular temporal profile. Three peening configurations were investigated in total. The main distinction between these configurations is whether a protective layer was (LSP) or was not (LPwC) applied and what kind of water confinement was utilized (thin water layer or water tank). In the experiment, every configuration is represented by a single set of selected laser parameters. The first configuration is the commonly utilized setup with protective coating in the form of a 100 μm black vinyl tape and a laminar thin layer of flowing water while using the 1030 nm infrared (IR) laser wavelength. This peening condition will be referred to as LSP IR. The setup is depicted in Fig. 1b. Pulses of 3 J were focused to a 2.6 mm square laser spot with resulting power density of 3.17 GW/cm^2. To prevent tearing of the tape, the pulses were delivered in a form of layers, each consisting of 4 sequences. A sequence comprised a 20 mm × 20 mm laser pattern with 0% overlap between individual laser spots. Subsequent sequences were shifted with respect to the first one in turn by 1.3 mm in X, Y, and XY direction in order to achieve 50% laser spot overlap within one layer. In total, 2 layers were applied to each LSP IR sample. The sample after peening is shown in Fig. 2a. The surface is clearly deformed but it retains its polished appearance. The second peening configuration involved similar setup with 1030 nm IR laser wavelength and thin water layer but with the protective coating removed. This condition will be referred to as LPwC IR. With the tape absent, the 20 mm × 20 mm patch was peened in a single pass using overlapping pulses with total pulse density of 1089 p/cm^2. The pulse energy was 1 J with a laser spot size of 1.5 mm. The power density was again 3.17 GW/cm^2. The sample after peening is shown in Fig. 2b with a thermally affected surface observable in the treated area. The third configuration involved peening with a sample submerged underwater with no protective coating applied. The underwater environment does not allow for the use of the standard 1030 nm due to its low transmission in water. Therefore, the second harmonic generation (SHG) at 515 nm was used. This condition will be referred to as LPwC SHG. The setup is depicted in Fig. 1c. The pulse energy was once again 1 J with laser spot size of 1.5 mm, power density of 3.17 GW/cm^2 and pulse density of 1089 p/cm^2. The LPwC SHG sample after treatment is shown in Fig. 2c. Similarly to LPwC IR, a white recast layer was created on the surface but it was less coarse and more uniform. The specimen labeling is summarized in Table 2. All treated specimens in this work were sensitized prior to peening.

After treatment, samples were measured via X-ray diffractometer (XRD) to determine surface residual stresses. The measurements were carried out using the RIGAKU AutoMATE II machine while utilizing the $\sin^2\psi$ method. The radiation used was Cr Kα (2.2897 nm) at $2\Theta = 139.3^\circ$.

Table 1
Chemical composition of AA5083-H116.

Element	Composition in wt%
Mg	4.0–4.9
Si	0.4
Mn	0.4–1.0
Fe	0.4
Other (Zn, Cr, Ti, Cu)	0.65
Al	balance

2.3. Electrochemical testing

All corrosion tests were carried out in a 3.5 wt% NaCl naturally aerated water environment at room temperature of 25 °C using a flat-cell with a platinum mesh counter electrode and a standard Ag/AgCl reference electrode. A Gamry ref 600+ potentiostat was used for all the measurements. Prior to testing, specimens were sealed with a silicon mask and sealant with a 15 mm circular opening in the middle to prevent crevice corrosion around the O-ring contact area. In potentiodynamic testing, the potential was scanned with a sampling period of

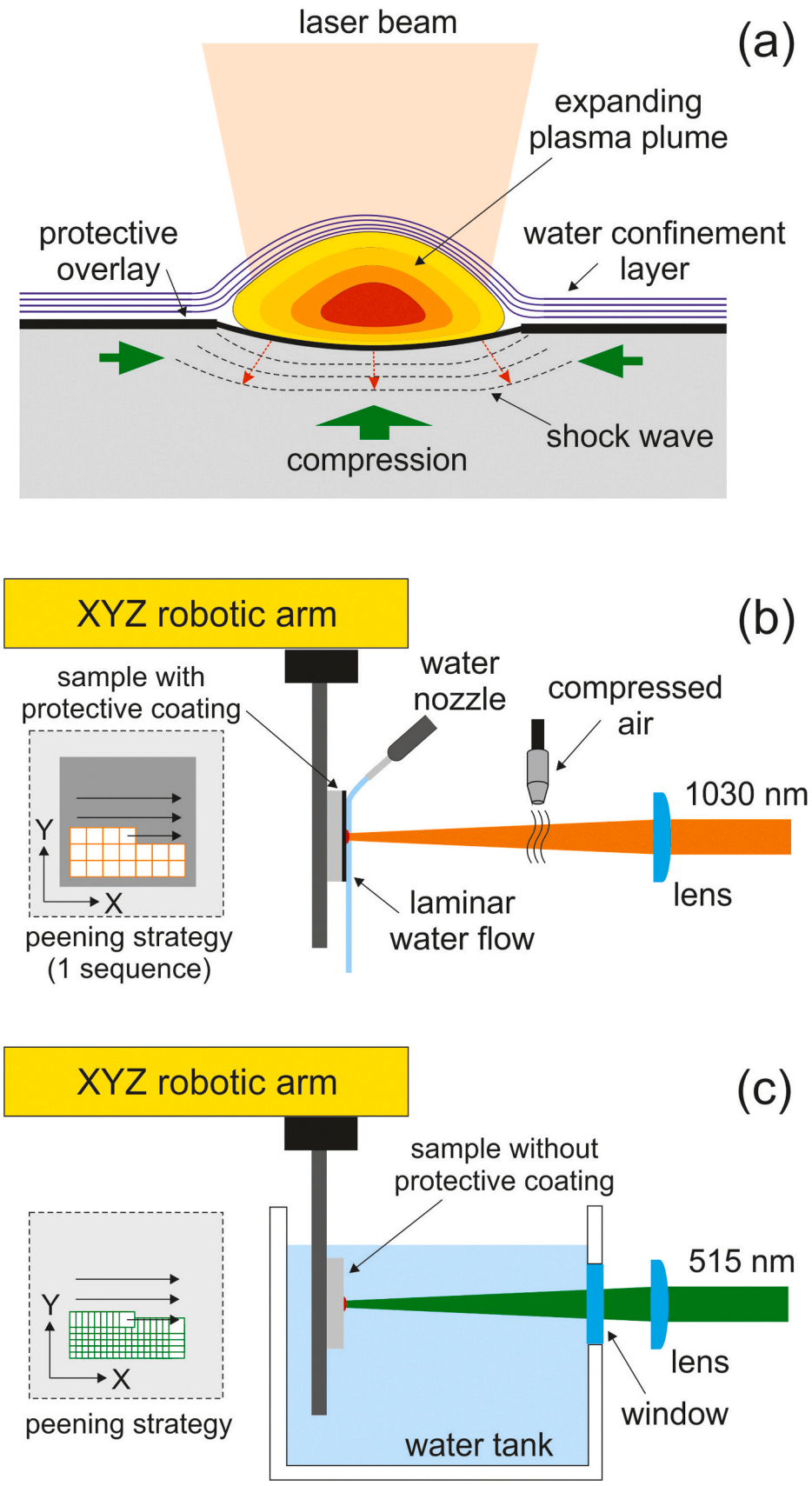


Fig. 1. (a) LSP scheme, (b) LSP treatment with protective coating applied and (c) LSP treatment without protective coating (LPwC) performed underwater.

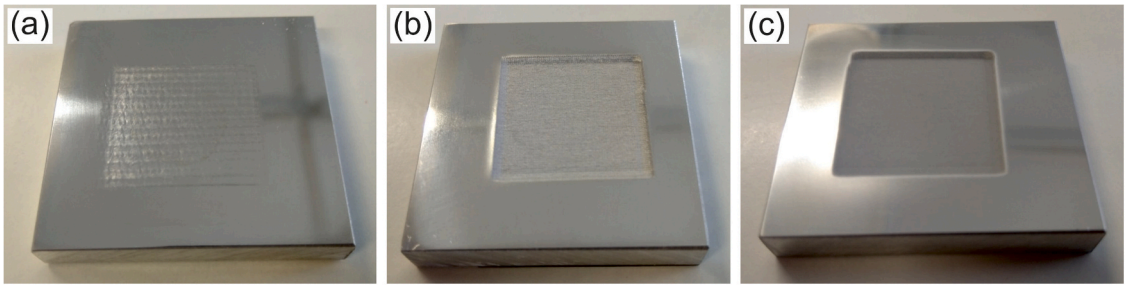


Fig. 2. Sensitized AA5083 specimens after treatment: (a) LSP IR, (b) LPwC IR and (c) LPwC SHG.

Table 2
Specimen labeling.

Specimen label	Sensitization	Treatment	Protective coating	Wavelength	Water confinement
AR (as received)	no	no	x	x	x
SE (sensitized)	yes	no	x	x	x
SE + LSP IR	yes	LSP	yes	1030 nm	1 mm water layer
SE + LPwC IR	yes	LPwC	no	1030 nm	1 mm water layer
SE + LPwC SHG	yes	LPwC	no	515 nm	water tank

0.33 mV/s. The current density was capped at 1 mA/cm^2. The scan started at 50 mV below the steady corrosion potential (E_{corr}) after a 30-minute stabilization period. Potentiostatic measurements involved polarization of the samples in their cathodic region at −800 mV vs Ag/AgCl with the current density being recorded for a period of 6 h. The same polarization level of −800 mV vs Ag/AgCl was applied during electrochemical impedance spectroscopy (EIS) testing with 5 mV RMS voltage oscillation and frequency range from 100 kHz down to 100 mHz. The recorded data series were fitted with an equivalent electrical circuit using ZSimWin software.

A fresh sample was used for each measurement with at least 3 measurements performed per sample condition. The plots presented in this paper are representative results of these replicated measurements.

2.4. Near-surface chemical analysis and microscopy

XPS analysis was carried out to investigate chemical composition of the modified specimen surfaces. A depth profile to differentiate between Al oxide and Al metal was obtained using a KRATOS AXIS Supra XPS instrument (sputtering by Ar+ ion clusters). The XPS spectra were acquired using a monochromatic Al Kα (1486.6 eV) X-ray source. The samples were subjected to 20 min of ion sputtering with an estimated sputtering depth of about 10 nm [24]. The number of Ar atoms in a cluster was 1000 and the energy of a cluster was 5 keV. The size of sputtered area was 2 mm × 2 mm.

Electron microscopy was employed to characterize the near-surface microstructure in a cross-sectional view. Samples were sectioned, fixed in an epoxy and polished with decreasing particle sizes down to 0.05 μm. The Scanning Electron Microscope (SEM) observations and lamella preparation were performed using ZEISS Auriga Compact instruments. Transmission Electron Microscopy (TEM) observations combining Energy Dispersive X-ray (EDX) elemental analysis were performed on a Jeol 2000FS TEM/STEM at an acceleration voltage of 200 kV.

3. Results

3.1. Surface morphology and residual stresses

Fig. 3 shows SEM images of the AA5083 surface before and after sensitization. Regions of grain boundary locally sensitized by the β-phase have been revealed by etching samples in 8.5 vol% H_3PO_4 at

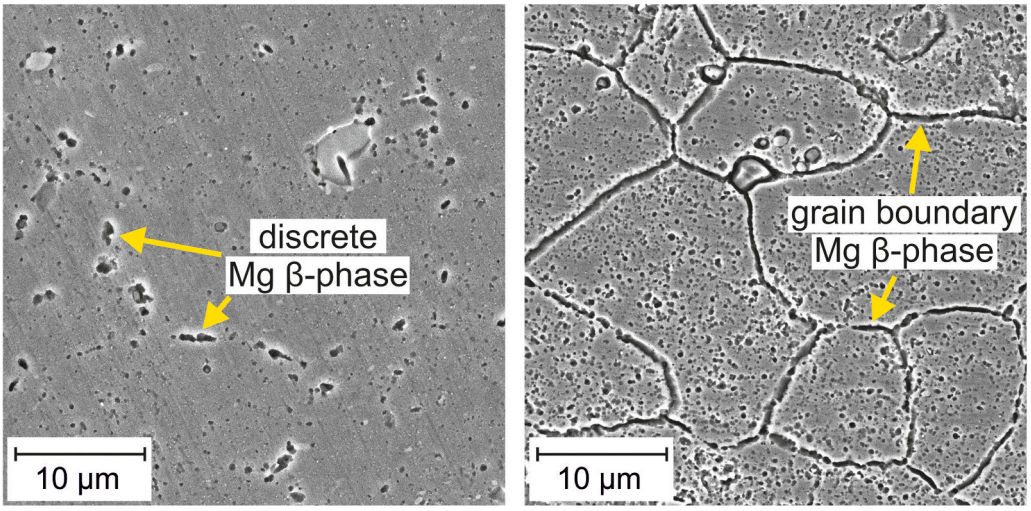


Fig. 3. SEM images of AA5083 after being etched in 8.5 vol% H_3PO_4 at 60 °C for 1 min (a) Rolling plane of as received material with discrete β-phase precipitates along the grain boundaries and (b) rolling plane of sensitized material with nearly continuous β-phase grain boundary network.

60 °C for a 1 min period [25]. The non-sensitized surface in Fig. 3a shows discrete instances of β-phase sensitization outlining individual grains of the material. In contrast, Fig. 3b shows the boundaries segments sensitized by the β-phase form a nearly continuous network through the sensitized specimen. The β-phase precipitates themselves are expected to remain discrete though densely populated under the particular sensitization conditions used, each sensitizing a region of the boundary much larger than their direct footprint [26]. The NAMLT results point to the sensitized sample being susceptible to IGC which is in accordance with literature, where the β-phase continuity is the primary factor behind high DoS [5].

Fig. 4 shows the surface condition of sensitized samples after treatment obtained by SEM using the backscatter electron detector (BSD). The non-treated surface is shown in Fig. 4a with intermetallic particles clearly visible. The surface after LSP IR is displayed in Fig. 4b. Slight deformations of the surface can be observed as a result of the peening process but no clear structural changes are apparent with the intermetallic particles still visible. Fig. 4c and d show the surface condition after LPwC IR and LPwC SHG, respectively. Both surfaces show distinct recast morphology as a result of the heat absorption during the laser pulse impact. The intermetallic particles are no longer visible.

Surface residual stresses measured on both treated and non-treated samples are shown in Table 3. For the treated samples, the measurement was carried out in 2 perpendicular directions, referred to as scanning (σ_S) and transversal (σ_T) with respect to the scanning direction during the peening process. The highest compressive stresses were achieved with LSP IR where a protective overlay was used. As expected, both LPwC samples showed lower compression due to heat affected recast layer on the surface caused by the laser pulse absorption. It is also worth noting the direction dependency of stress in the LPwC samples with higher σ_T stresses, consistent with other publications where LPwC was employed [11,15]. Non-treated samples show negligible compression in comparison.

3.2. Potentiodynamic testing

Prior to treatment, the effect of sensitization in terms of thermodynamic stability was evaluated by potentiodynamic polarization measurement. Fig. 5 shows potentiodynamic curves of as received and sensitized AA5083 in a 3.5 wt% NaCl solution. Both curves exhibit similar shape with an offset along the applied potential. The as received sample displays nobler E_{corr} of −767 mV in contrast to −792 mV of the sensitized material. The anodic region in both cases is characterized by

Table 3
Surface residual stress measurement in laser scanning (σ_S) and transversal direction (σ_T).

Sample	σ_S (MPa)	σ_T (MPa)
AR	-28 ± 7	-9 ± 17
SE	-3 ± 6	-16 ± 15
SE + LSP IR	-170 ± 9	-169 ± 5
SE + LPwC IR	-40 ± 2	-149 ± 4
SE + LPwC SHG	-109 ± 3	-180 ± 3

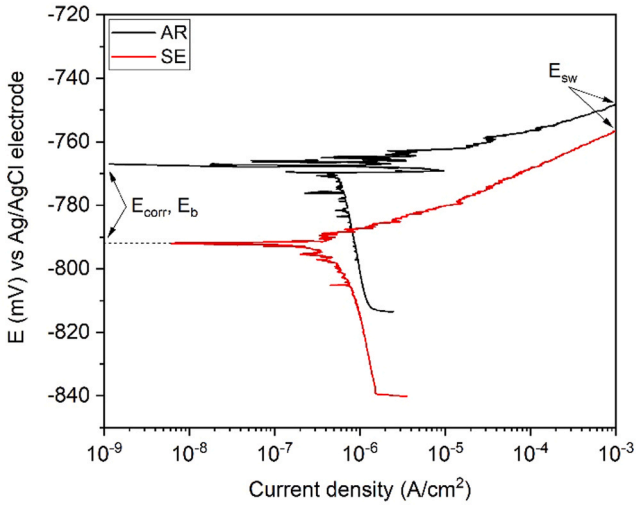


Fig. 5. Potentiodynamic polarization curves of as received and sensitized AA5083 in 3.5% NaCl solution.

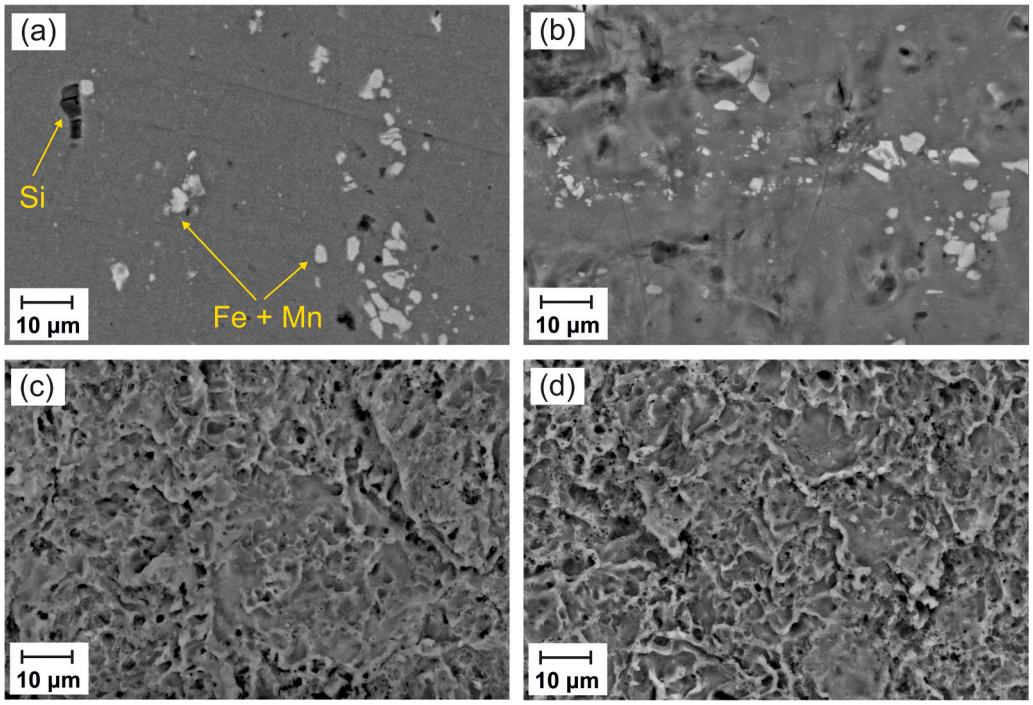


Fig. 4. SEM BSD surface images of sensitized samples before and after treatment: (a) non-treated, (b) LSP IR, (c) LPwC IR and (d) LPwC SHG.

sharp increase in current density with rising potential. The surfaces of as received and sensitized samples after the test are shown in Fig. 6a and b, respectively. Both surfaces display localized pitting attack which is more widespread in the case of sensitized sample. The lower pitting potential of the sensitized sample is attributed to galvanic coupling effects along the exposed β-phase grain boundaries.

Fig. 7 shows potentiodynamic measurements of sensitized samples under various treatment conditions. E_{corr} dropped in all cases when compared to the non-treated sample with the highest drop of 47 mV for the LSP IR sample. Both LPwC treatments, however, display extended passivity region with reduced anodic current. In these cases, E_b is shifted further away from E_{corr}, exceeding E_b of the non-treated sensitized sample by more than 20 mV. In contrast, the anodic region stayed relatively flat for LSP IR although slight indication of passivity may also be observed. This suggests that the kinetics of the process is controlled by oxygen diffusion through the porous oxygen film which is more developed after the LPwC treatment. The widespread pitting attack on the LSP IR surface (Fig. 6c) was similar to the non-treated sensitized sample (Fig. 6b). In contrast, the surface of the LPwC SHG sample (Fig. 6d) shows more localized pitting which penetrates the transformed recast layer. The polarization resistance R_p of the investigated samples was determined using the Linear Polarization Resistance method (LPR). Small voltage variations (±5 mV) were applied around E_{corr} and the slope of current response was measured. The resultant R_p values are summarized in Table 4 along with other characteristic dissolution parameters. Smaller electrical current variations and rapid increase in R_p were observed for the LPwC samples. Most notably nearly 50 times higher R_p was measured for LPwC SHG sample when compared to the non-treated sensitized sample (202.5 kΩ versus 4.3 kΩ). An increase in R_p, although much smaller, was also measured with the LSP IR sample.

3.3. Potentiostatic testing

In order to suppress the chloride driven attack, the samples were

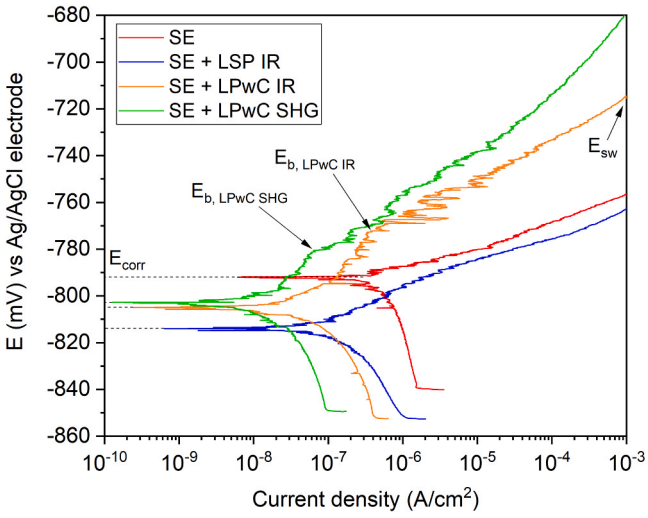


Fig. 7. Potentiodynamic polarization curves of treated sensitized AA5083 in 3.5% NaCl solution.

Table 4
Characteristic dissolution parameters obtained from potentiodynamic curves in 3.5% NaCl solution.

Sample	E_{corr} (mV)	E_b (mV)	E_{sw} (mV)	R_p (kΩ)
AR	-767	-763	-748	1.7
SE	-792	-788	-757	4.3
SE + LSP IR	-814	-814	-763	20.9
SE + LPwC IR	-805	-772	-715	70.1
SE + LPwC SHG	-803	-781	-680	202.5

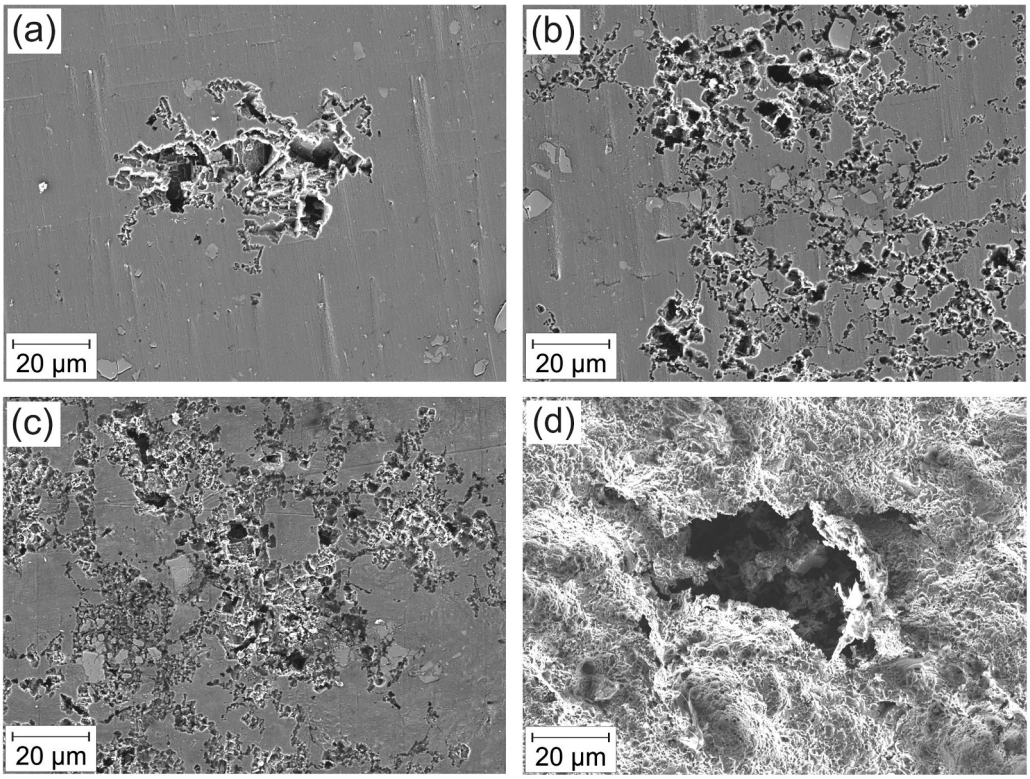


Fig. 6. SEM images of corrosion attack after potentiodynamic test: (a) as received sample, (b) sensitized sample (c) sensitized sample treated by LSP IR and (d) sensitized sample treated by LPwC SHG.

polarized at −800 mV vs Ag/AgCl, about 10 mV below E_{corr} of the sensitized material as determined by the potentiodynamic measurements [27]. The current density measured over time is shown in Fig. 8. In both non-treated cases, the current density starts in negative values as expected due to the cathodic polarization. After some time, the current density of the sensitized samples starts rising exponentially, reaching a value of 330 μA/cm^2 over a period of 6 h. On the contrary, the current density of the as received sample stays close to zero and does not deviate over time. The surface condition after the measurement is shown in Fig. 9. The as received sample (Fig. 9a) shows no signs of IGC after 6 h of immersion. In contrast, the sensitized sample (Fig. 9b) exhibits a distinct interconnected network of IGC all over the exposed surface area.

When it comes to the treated samples, both LPwC treatments show significant drop in current density. For LPwC IR, the current density after 6 h is 80 μA/cm^2 which is more than four times lower than in the case of the non-treated sensitized sample. For LPwC SHG, the current density after 6 h is 5 μA/cm^2, which is nearly the same as that of the as received sample. We can however assume that the current density will keep on rising albeit at an extremely slow rate when compared to the non-treated sensitized condition. LSP IR sample with protective coating showed only a slight improvement with final current density of 267 μA/cm^2 although for more than 3 h the curve practically copied that of the control sensitized sample which indicates that no significant change took place. This time, the current density starts in positive values as the LSP treatment lowers E_{corr} and thus the polarization takes place slightly above E_{corr} in the anodic region. The surface of LSP IR in Fig. 9c shows developing IGC network with most seriously corroded area in the middle. The LPwC SHG sample in Fig. 9d, on the other hand, shows no observable intergranular features. Instead, the corrosion manifests in the form of localized surface perturbations.

3.4. Electrochemical impedance measurement

The results of electrochemical impedance spectroscopy (EIS) are presented in the form of Bode and Nyquist plots in Figs. 10 and 11, respectively. The measurements were taken at a polarization potential of − 800 mV vs Ag/AgCl in 3.5 wt% NaCl which was shown to successfully isolate IGC from pitting corrosion. The Bode plot in Fig. 10 includes both the absolute impedance $|Z|$ and the phase shift of all 5 studied conditions, two of them being without and three with treatment. Two time constants can be distinguished, one in the high frequency range (~20–100 Hz) and one in the low frequency range (0.1–0.3 Hz). In the high frequency range, the plot indicates higher $|Z|$ for treated samples

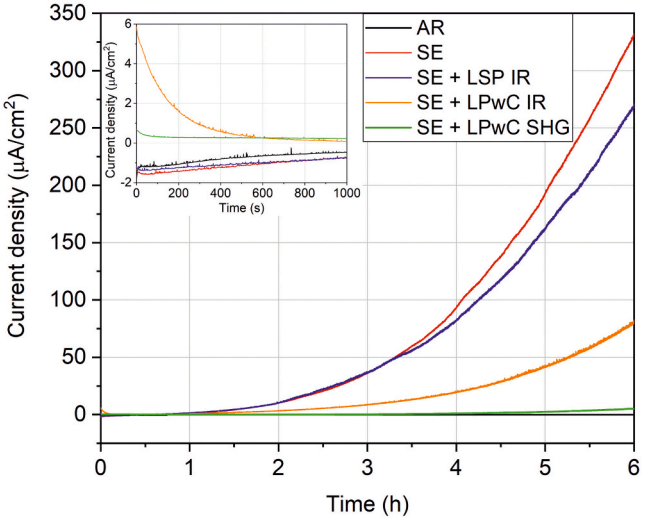


Fig. 8. Current density during potentiostatic polarization at −800 mV vs Ag/AgCl electrode of non-treated and treated AA5083 in 3.5% NaCl solution.

with protective coating as well as non-treated samples, both as received and sensitized. However, as we approach lower frequencies (< Hz), the trend is reversed and higher $|Z|$ is achieved with both LPwC conditions, LPwC SHG in particular. In contrast, specimens processed by LSP IR fall more than an order of magnitude behind. The phase angle shift data shows significant phase angle peak broadening for both LPwC conditions while the regular LSP IR peak narrows in comparison with the non-treated conditions. The peak broadening is indicative of a stable protection barrier spread across wider frequency range [20]. The Nyquist plots presented in Fig. 11 are in the form of semicircles with centers depressed below the x-axis. It can be seen that the LPwC specimens display higher resistance, represented by wider arc, when compared to the non-treated specimens. The LSP IR condition with protective coating shows the smallest arc, indicating lower resistance when compared to the rest of the tested conditions.

An impedance plot obtained for a given electrochemical system can be modeled by one or more equivalent electrical circuits [28] where the appropriate model gives a reasonable fit with the least amount of circuit components. In this case, an equivalent electrical circuit model $R_s(Q_c(R_{po}(Q_{dl}R_{ct})))$ was used based on the work of several authors [19, 29,30] who proved it to be adequate for modeling of aluminum corrosion. The model comprises two time constants as previously indicated by the potentiodynamic measurements and by the Bode and Nyquist plots. The high-frequency time constant is related to the reactions at the outer interface ($R_{po}Q_c$), i.e. the porous oxide film and electrolyte where R_{po} represents the film pore resistance and Q_c the film capacitance or constant phase element CPE. CPE is used to signify the possibility of a non-ideal capacitance with a varying n. The factor n is within the range of $0 \leq n \leq 1$. When $n = 1$, Q describes an ideal capacitor. The value of n is related to the electrode roughness and heterogeneities [31]. The second time constant at low frequencies ($R_{ct}Q_{dl}$) is attributed to the charge-transfer reaction at the metal surface (inner barrier), in the base of the oxide film pores where R_{ct} and Q_{dl} represent the charge transfer resistance and double layer capacitance, respectively. The electrolyte resistance is denoted by R_s. A good fit of the experimental data was achieved and the results are shown in Table 5.

According to the data, the combined resistance R_s+R_{po}+R_{ct} of the LPwC SHG treatment increased more than 3 times (178 ± 16 kΩ) when compared to non-treated sensitized sample SE (58 ± 24 kΩ). This suggests that the underwater treatment increased both the quality of the oxide film (R_{po}) as well as the passivity of the transformed layer below (R_{ct}). Lower R_{ct} of the non-treated and LSP IR specimens generally indicates an increase in the metal area in contact with the electrolyte, denoting the penetration of water molecules, oxygen anions through the porous film, and the corrosion activity on the metal surface [32]. The large difference between LPwC IR (33 ± 5 kΩ) and LPwC SHG (87 ± 38 kΩ) in R_{po} is attributed to the surface oxide film quality which tends to be more uniform in case of underwater treatment. These results are in good agreement with the potentiodynamic measurements from Fig. 7. On the other hand, LSP IR underperformed heavily when compared with the non-treated SE condition, with the combined resistance of only 8.0 ± 0.2 kΩ. This result suggests that the treatment with protective coating in this case does have a negative effect on the oxide film. The discrepancy between this result and the higher R_p value compared to SE sample (Table 4) can be attributed to the anodic dissolution of LSP IR polarized at −800 mV vs Ag/AgCl during EIS.

The highest Q_c was achieved with LPwC IR which suggests increased surface porosity and heterogeneity. In contrast, lower Q_c of LSP IR compared to the non-treated SE sample points to more homogenous surface layer after laser treatment with protective coating. In addition, Q_{dl} of the treated samples was significantly lower when compared to the non-treated samples. The decrease in Q_{dl} of the metal surface/solution interface after laser treatment is probably an outcome of lower ion adsorption due to more difficult penetration of water molecules, oxygen, and Cl^- ions [19,33]. The values of n-Q_c and n-Q_{dl} are in the range of 0.94–1.00; hence Q_c and Q_{dl} can be considered approximately as a pure

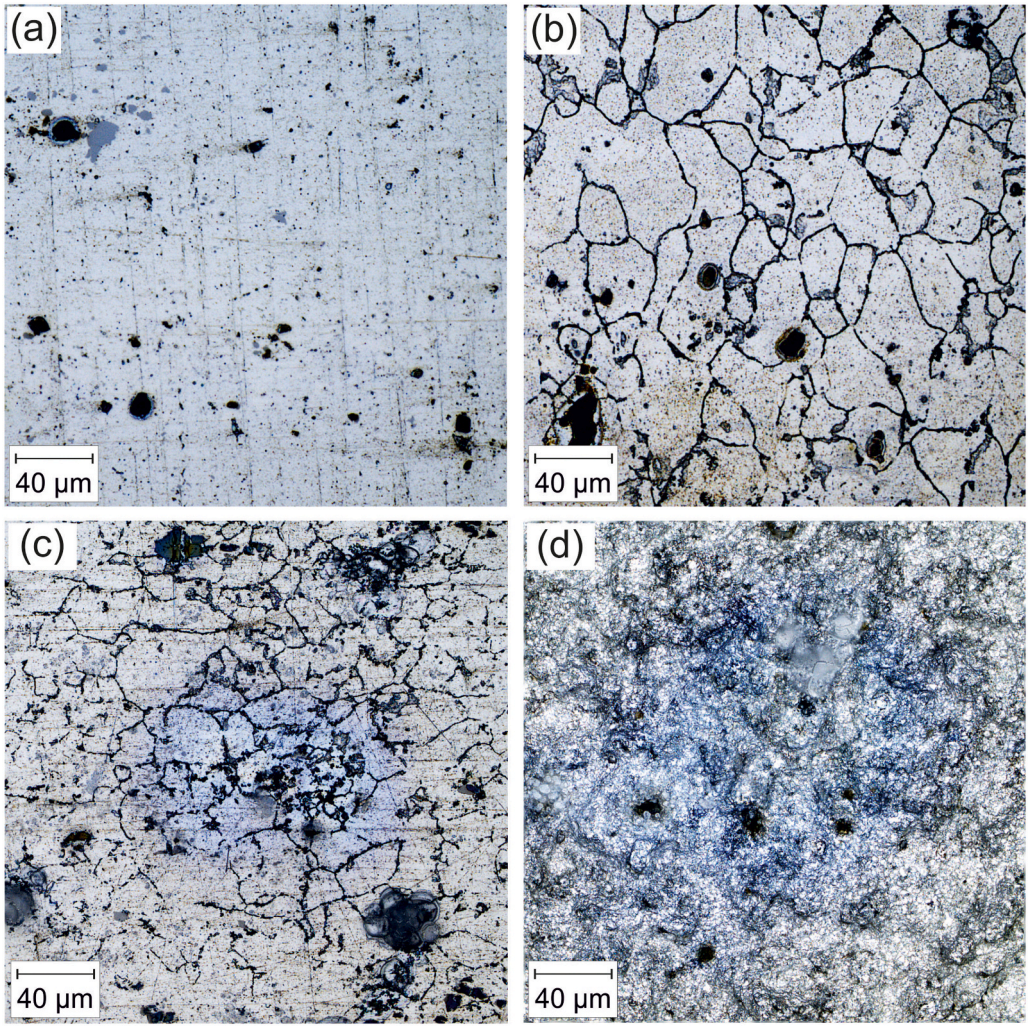


Fig. 9. Optical microscope images of AA5083 after potentiostatic polarization at −800 mV vs Ag/AgCl for 6 h: (a) as received, (b) sensitized sample with developed IGC network, (c) LSP IR, (d) LPwC SHG.

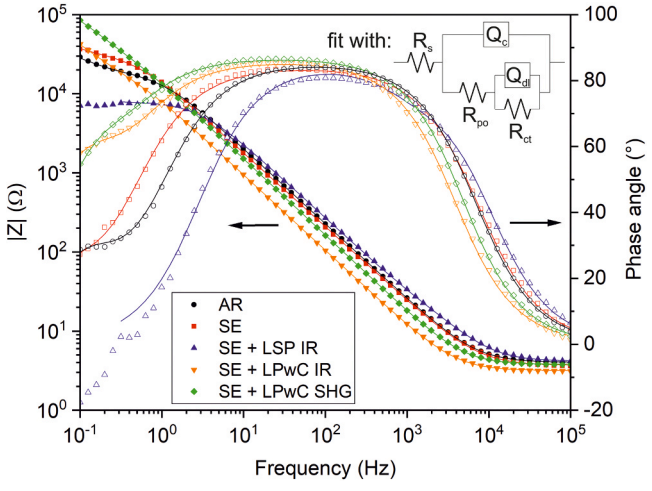


Fig. 10. EIS spectra recorded in 3.5 wt% NaCl represented by Bode plot. The absolute impedance plot is represented by filled data points and the phase angle by open data points. The plots were fitted using the displayed equivalent electrical circuit.

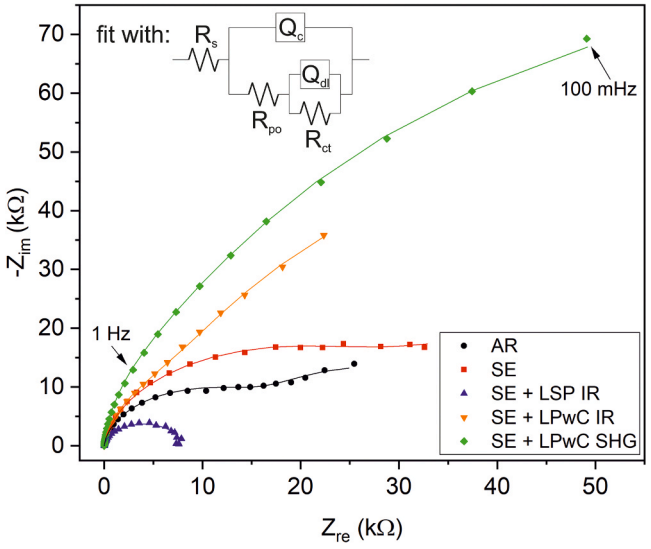


Fig. 11. EIS spectra recorded in 3.5 wt% NaCl represented by Nyquist plot. The data is fitted using the displayed equivalent electrical circuit.

Table 5
Electrochemical parameters obtained from EIS spectra.

Sample	R_s (Ω cm^2)	R_{po} (kΩ cm^2)	R_{ct} (kΩ cm^2)	Q_c (μF cm^{-2})	n-Q_c	Q_{dl} (μF cm^{-2})	n-Q_{dl}
AR	4.0	21 ± 1	20 ± 5	5.0 ± 0.1	0.95	53.0 ± 4.1	1.00
SE	3.7	36 ± 2	21 ± 24	7.0 ± 0.2	0.94	75.0 ± 21.9	1.00
SE + LSP IR	4.2	0.1 ± 0.1	7.9 ± 0.2	4.0 ± 1.5	0.95	1.0 ± 1.5	0.94
SE + LPwC IR	3.2	33 ± 5	87 ± 38	11.0 ± 0.3	0.96	15.0 ± 1.7	0.95
SE + LPwC SHG	3.8	80 ± 8	98 ± 14	7.0 ± 0.1	0.97	7.0 ± 1.2	0.96

capacitors.

3.5. XPS analysis

Spectra of Al 2p were measured and fitted with Gaussian functions to distinguish between states corresponding to different bonding energies. The ratio of areas inside the recorded peaks then represents the ratio of corresponding components present in the material. The two main components revealed were Al-oxide Al_2O_3 at 75.7 eV and Al-metallic at 72.5 eV. One of the spectra, specifically LPwC SHG at 10 nm, is shown in Fig. 12a. Other spectra are similar, with varying ratios of the Gaussian areas. The ratios of calculated areas of Al_2O_3 oxide to metallic Al in Al 2p spectra are plotted in Fig. 12b. Each sample condition is represented by 2 columns, one with no argon sputtering representing the sample surface and second after 20 min of sputtering which corresponds to a depth of 10 nm. Both non-treated conditions show a similar ratio of the oxide and metallic Al on the surface. At the estimated depth of 10 nm, the amount of Al_2O_3 decreases with depth due to less oxygen molecules being present further away from the surface. This drop is more pronounced with the as received sample at 85–78% as opposed to the 83–81% of the sensitized sample. In the case of treated samples, the largest difference can be observed with the LPwC samples. The amount of Al-metallic was halved when compared to the non-treated conditions while the amount of Al_2O_3 increased correspondingly. LSP IR showed no increase in Al-oxide but rather the lowest amount of all the conditions tested with 82% on the surface and 76% at 10 nm.

3.6. Microstructure analysis

Near-surface cross-section SEM images of the treated specimens are shown in Fig. 13. The smooth LSP IR surface in Fig. 13a contrasts with the LPwC SHG surface in Fig. 13b where a recast layer approximately 2–3 μm thick with a modified oxide layer on top can be observed. The etched cross section of the LSP IR sample (Fig. 13c) further reveals β-phase sensitized grain boundaries in very close proximity to the surface. In case of the etched LPwC SHG sample (Fig. 13d), however, the sensitized boundaries are shielded from the surface by the recast layer that was generated during the laser pulse interaction when no protective coating was applied.

Fig. 14 provides a closer look at the near-surface cross-section of the sensitized material without treatment. The TEM image in Fig. 14a shows that the polishing process creates fine flat grains up to a depth of about 100 nm. These grains are divided into several subgrains containing high dislocation density. Underneath, larger grains are also heavily deformed as a result of the manufacturing process. Fig. 14b and c then show the Mg precipitates distribution both in coarse isolated particles as well as dense coverage on the grain boundary. The subgrains are subjected to large stress with high dislocation density homogeneously distributed in the volume with Fe and Mn precipitates present.

When the plate was treated with the protective coating applied (LSP IR), most of the grains near the surface were refined (Fig. 15a). The newly formed subgrains contain high dislocation density (Fig. 15c) and the affected zone reaches up to 300 nm below the surface. There is no grain boundary β-phase in this region (Fig. 15b), however, below this region the structure is the same as in the initial sensitized state. This means that the shock wave induced plastic deformation can dynamically change the microstructure only to a limited depth. The presence of Mg enrichment at the boundary of this refined layer is interesting, as well as the morphological transition of the β-phase to what appears to be a smooth film, as opposed to the less uniform thickness observed in Fig. 14b that is typical of a densely populated but largely discrete β-phase coverage viewed in transmission. The limited area of the TEM sample, however, makes it hard to discern how prevalent this phenomenon is.

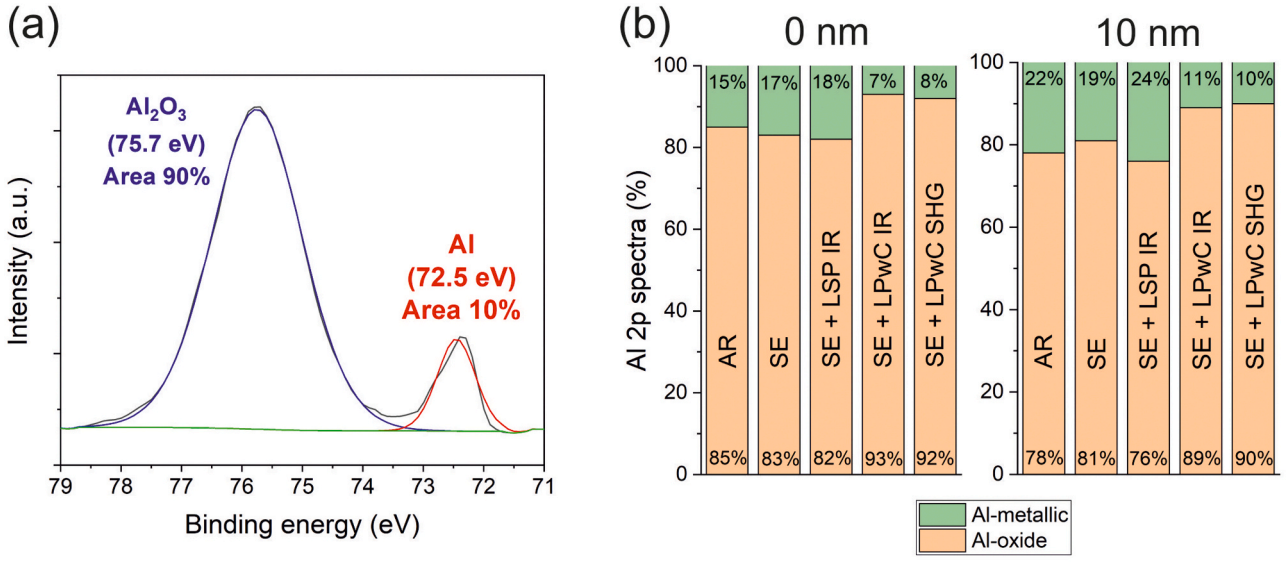


Fig. 12. XPS analysis of bonding energies: (a) Al 2p spectrum of LPwC SHG at a 10 nm depth and (b) the ratio of Al-metallic and Al-oxide of non-treated and treated specimens at 0 nm and 10 nm depth.

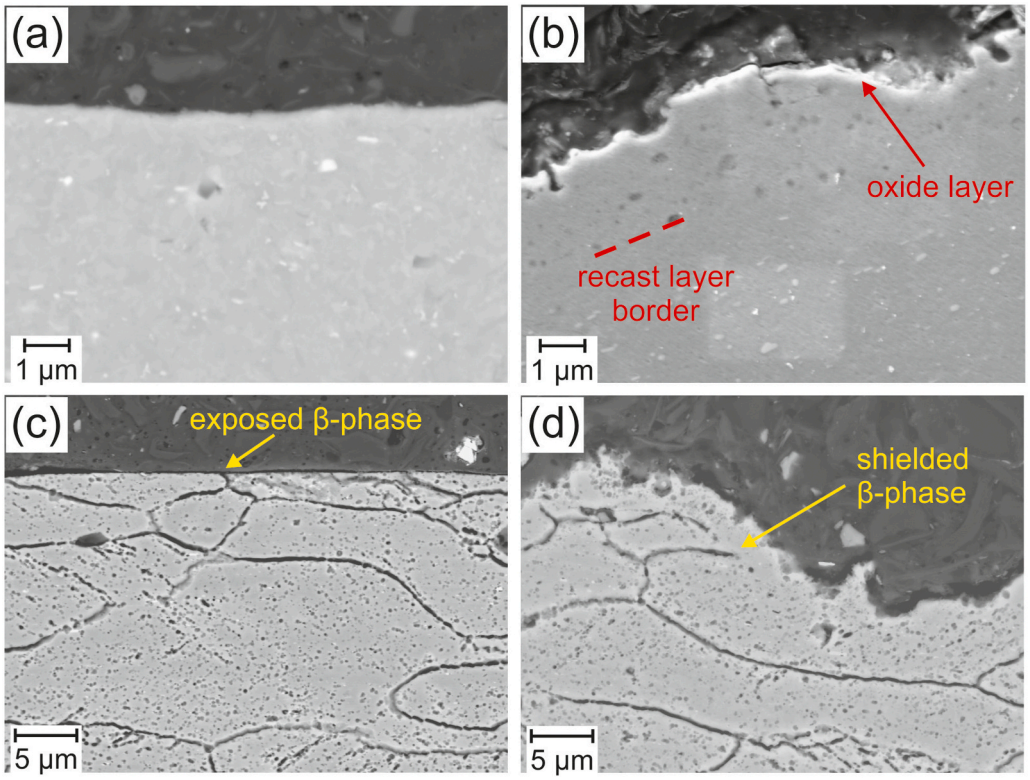


Fig. 13. SEM cross section images of treated sensitized AA5083: (a) LSP IR, (b) LPwC SHG with recast layer and modified oxide layer visible, (c) LSP IR with β-phase visualized, (d) LPwC SHG with β-phase visualized and shielded from the surface.

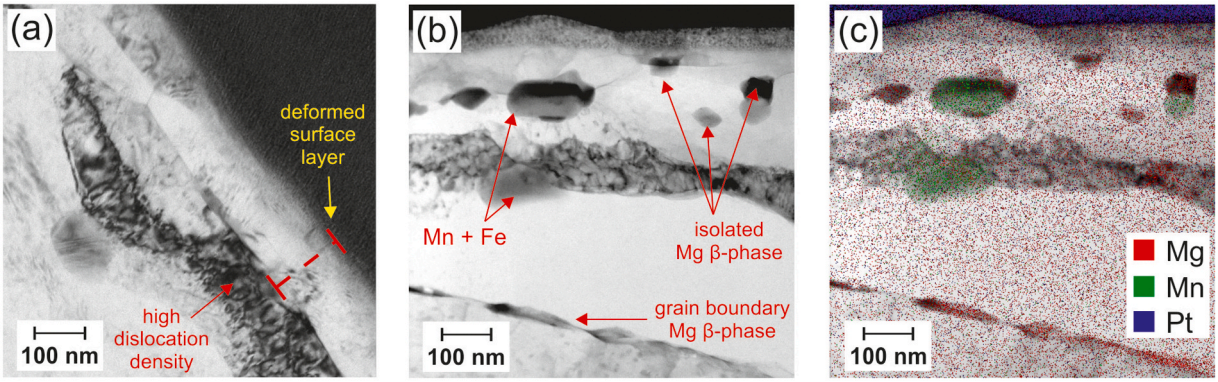


Fig. 14. Cross-section images of near-surface area of sensitized AA5083 with no treatment applied: (a) TEM of the surface layer deformed by polishing, (b) STEM image of particles near the surface and (c) distribution map of selected elements.

The microstructure observed in the surface region of the LPwC SHG sample (Fig. 16) is very different from that of both non-treated and LSP IR samples. First, a nearly 2–3 μm wide recast surface layer is present (Fig. 16a) which is quite different from that of the base material beneath this region seen below the white dashed line in the TEM image. The β-phase precipitates that appear dark in the BF image and brighter in STEM EDS Mg map in Fig. 16b have been taken back into solution in the melted and recast layer that appears in a uniform gray contrast; the STEM EDS map in Fig. 16b reveals the β-phase distinctively, but also that the Mg is evenly distributed in the recast layer. The second remarkable feature is the presence of numerous nanoparticles of varying size embedded within this layer. Very recent work on LPwC of Al7075-T6 alloy has determined that these are oxygen-rich aluminum nanoparticles [34], and possible mechanisms for their formation have been discussed. The recast layer and the layer below are also marked by a heavily deformed structure with high dislocation density and subgrain boundaries (Fig. 16a and c). This microstructure reaching into the depth is the result of shock-assisted deformation. Overlapping laser spots result in heterogeneous thermal and mechanical conditions, which consequently lead to further increase in dislocation density and less defined subgrains. These subgrains are kept under stress caused by rapid solidification and by compressive residual stresses. Since the LPwC SHG sample was processed in water environment without protective coating, the aluminum nanoparticles in Fig. 16a are enriched in oxygen. The melting/solidification and thermomechanical deformation mechanism during LPwC led to dissolution of β-phase precipitates at original grain boundaries and more uniform distribution of Mg in solution in the recast surface layer (Fig. 16b), as well as their break-up into coarser precipitates in the matrix regions below (Fig. 16c).

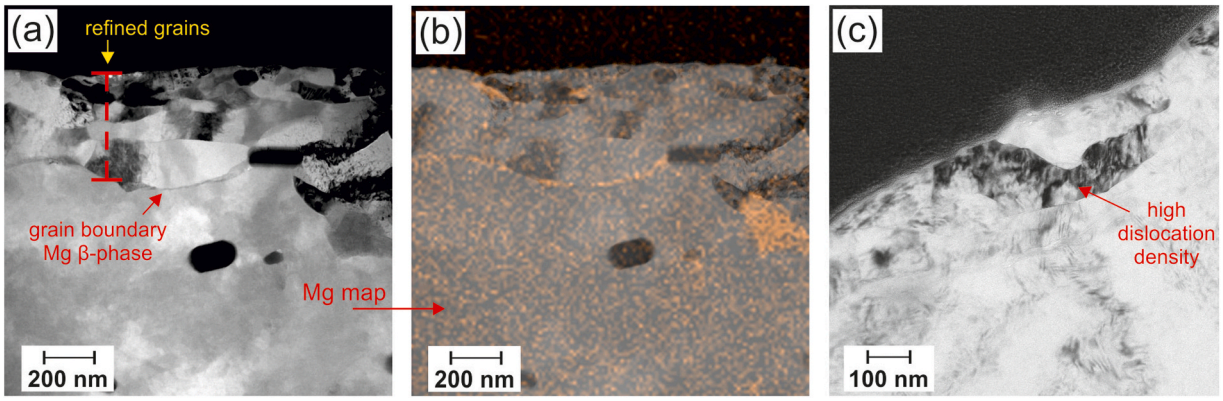


Fig. 15. Cross-section images of near-surface area of sensitized AA5083 after LSP IR treatment: (a) STEM of LSP induced subgrains, (b) Mg distribution in the surface region and (c) TEM showing detail of the subgrains with high dislocation density.

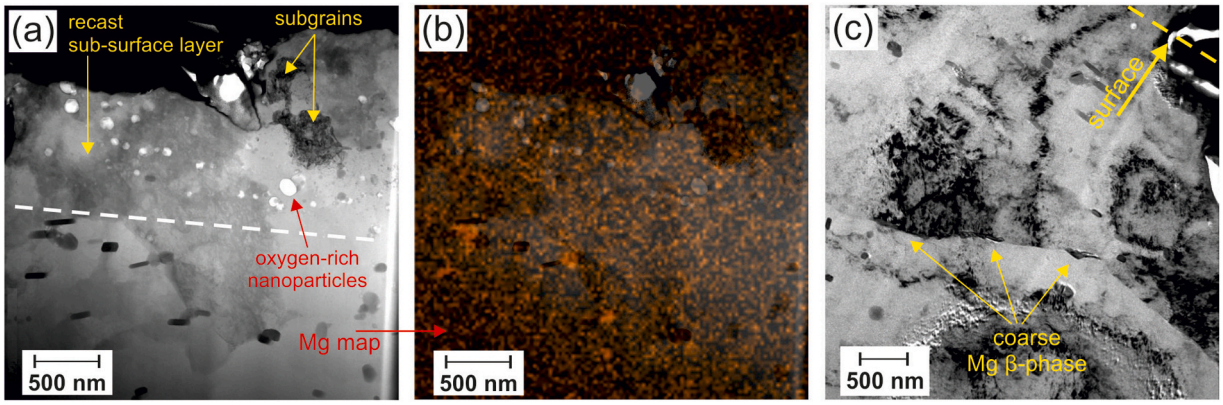


Fig. 16. Cross-section images of near-surface area of sensitized AA5083 after LPwC SHG treatment: (a) TEM showing the uniform solid solution recast layer with embedded oxygen-rich Al nanoparticles, (b) Mg map of the recast layer and (c) STEM of coarse β-phase precipitates under the recast layer.

4. Discussion

While the LSP technology is predominantly employed to prolong fatigue lifetime of aluminum alloys by generating compressive residual stresses [16,35–38], both the results of the present work and previous reports indicate that the corrosion performance can also be improved. Our findings show that while all the LSP based treatment methods used in this work generate plastic strain and compressive residual stresses (Table 3), the effect on corrosion resistance varies depending on whether an ablative overlay is applied or not, with other processes that affect the near-surface microstructure such as melting, solidification, surface oxide formation and grain refinement also playing significant role. In general, corrosion behavior of aluminum alloys is determined by the behavior of the surface oxide film, notably its degree of hydration and porosity [39]. The film forms either naturally or through thermodynamic processes. In spite of the LSP IR sample displaying the highest combined compressive stresses, the process is purely mechanical and thus no modified oxide layer is generated. Although some improvement was observed in R_p (Table 4), the data suggests that the character of the oxide film stayed mostly unchanged when compared to the LPwC treatments. This is further supported by the XPS analysis (Fig. 12b) where similar or slightly lower amount of aluminum oxide compared to non-treated samples was detected. Instead, the grains to about 300 nm depth are refined (Fig. 15a) which is consistent with other publications which showed that the thickness of the LSP refined aluminum microstructure is usually only about 200 nm [17,40,41]. Despite no β-phase being present around the newly formed grain boundaries (Fig. 15b), the potentiostatic measurement in Fig. 8 suggest that this newly refined layer does not have an effect on IGC. This could be possibly due to low thickness of the refined layer since according to Seong et al. [27], 1 μm thick altered layer with refined grains is already sufficient to affect IGC.

During the LPwC treatment, on the other hand, the direct interaction between the nanosecond laser pulse and the aluminum alloy surface under a water confinement creates a modified oxide layer and underlying transformed recast layer with a microstructure composed of a supersaturated Al solid solution free of β-phase precipitates, combined with a high dislocation density. These features are the result of the combined effect of thermal (melting/solidification) and high pressure severe plastic deformation as the pressure and temperature present are in the order of GPa [22,42] and thousands of °C [43], respectively. The presence of the modified oxide layer is supported by the XPS analysis (Fig. 12b) where higher amount of aluminum oxide was detected as well as by potentiodynamic measurements (Fig. 7) where larger regions of passivity were observed. R_p after LPwC treatment was significantly increased which is in accordance with literature [19,20,44] where the improved corrosion characteristics of aluminum were attributed to modified oxide layer resulting from the LPwC process. Furthermore, the microstructure analysis gave evidence for β-phase free Al solid solution with high dislocation density layer beneath (Fig. 16). The 2–3 μm thick recast layer acts as a shielding barrier between the underlying β-phase and the electrolyte (Fig. 13d). This resulted in significantly lower IGC current measured during the potentiostatic test (Fig. 8) and higher resistance in the EIS analysis (Table 5). Furthermore, the recast layer being a uniform solid solution free of β-phase precipitates along the grain boundaries considerably minimizes galvanic coupling effects, mitigating early pitting by the electrolyte. Lastly, the increased roughness of treated samples means that the area exposed to the electrolyte is actually higher than area of the non-treated samples. This means that the

corrosion current density of treated samples should objectively be even lower than presented here which further supports the conclusion of positive impact of LPwC.

5. Conclusion

In this work, the effect of LSP and LPwC treatment on IGC of sensitized AA5083-H116 was investigated. Three distinct peening configurations were used, one with protective overlay and two without which were further separated by different water confinement. The specimens were subjected to a series of electrochemical tests and microstructural analysis. The following conclusions can be made:

1) Compressive residual stresses were found on the surface of all treated specimens together with a modified microstructure. The highest compressive stresses (−170 MPa) were achieved by LSP with protective coating.
2) Laser plasma interaction with the aluminum surface associated with the LPwC process creates β-phase free, supersaturated Al solid solution recast layer with a modified oxide layer on top in the treated area. This leads to the creation of a passive region with significantly lower anodic current in the potentiodynamic measurement.
3) The modified oxide layer and the 2–3 μm thick β-phase free recast layer from the LPwC treatment shield the underlying β-phase regions from the electrolyte which results in significantly reduced IGC current during potentiostatic measurements, most notably for LPwC performed underwater.
4) Despite 300 nm of refined microstructure caused by LSP with no grain boundary β-phase present, the low thickness is not sufficient to protect the specimen against IGC.
5) EIS measurements showed significantly improved corrosion resistance for both LPwC specimen while LSP treatment with protective coating showed reduction in corrosion resistance when compared to the non-treated sample.

We have shown that the LPwC treatment, especially underwater, has a positive effect on suppressing IGC in sensitized AA5083. Combined with the added benefit of deep compressive residual stresses, LPwC could be a promising technique in combating IGSCC in the marine industry. Future steps could possibly involve more detailed investigation into the underwater LPwC treatment specifically with more varying parameters taken into account.

CRediT authorship contribution statement

Jan Kaufman: Conceptualization, Methodology, Investigation, Writing – original draft, Visualization. **Jan Racek:** Methodology, Investigation, Writing – review & editing. **Miroslav Cieslar**: Validation, Writing – review & editing. **Peter Minarík:** Validation, Writing – review & editing. **Matthew A. Steiner:** Conceptualization, Validation, Writing – review & editing, Funding acquisition. **Seetha R. Mannava:** Resources, Supervision, Funding acquisition. **Vijay K. Vasudevan:** Conceptualization, Validation, Writing – review & editing, Funding acquisition. **Anurag Sharma:** Resources. **Marek Böhm:** Resources. **Jan Brajer:** Supervision. **Jan Pilař:** Resources. **Ladislav Pína:** Supervision. **Tomáš Mocek:** Funding acquisition.

Declaration of Competing Interest

The authors declare that they have no known competing financial interests or personal relationships that could have appeared to influence the work reported in this paper.

Data availability

The raw/processed data required to reproduce these findings cannot be shared at this time due to technical or time limitations.

Acknowledgements

This work was supported by European Structural and Investing Funds, Operational Programme Research, Development and Education (Grant agreement NO CZ.02.1.01/0.0/0.0/15_006/ 0000674) and from the European Union's Horizon 2020 research and innovation programme (Grant agreement NO 739573). JK, AS, MAS, SRM and VKV would also like to express our gratitude to the Ohio Department of Development and Third Frontier Commission (Grant # TECH 10-014), which provided funding in support of the "Ohio Center for Laser Shock Processing for Advanced Materials and Devices" and the equipment in the center that was used in the initial part of this work.

References

[1] R. Zhang, S.P. Knight, R.L. Holtz, R. Goswami, C.H.J. Davies, N. Birbilis, A survey of sensitization in 5xxx series aluminum alloys, Corrosion 72 (2016) 144–159, https://doi.org/10.5006/1787.
[2] R.K. Gupta, R. Zhang, C.H.J. Davies, N. Birbilis, Influence of Mg content on the sensitization and corrosion of Al-xMg(-Mn) alloys, Corrosion 69 (2013) 1081–1087, https://doi.org/10.5006/0948.
[3] Y. Zhong, M. Yang, Z.-K. Liu, Contribution of first-principles energetics to Al–Mg thermodynamic modeling, Calphad 29 (2005) 303–311, https://doi.org/10.1016/j.calphad.2005.08.004.
[4] N. Birbilis, R.G. Buchheit, Electrochemical characteristics of intermetallic phases in aluminum alloys, J. Electrochem. Soc. 152 (2005) B140, https://doi.org/10.1149/1.1869984.
[5] G. Yi, Y. Zhu, E. Sundberg, A.T. Derrick, M.L. Free, Sensitization prediction and validation for Al 5xxx alloys exposed to long-term cyclical and constant heating at low temperatures, Corrosion 72 (2016) 177–186, https://doi.org/10.5006/1918.
[6] C.B. Crane, R.P. Gangloff, Stress corrosion cracking of Al-Mg alloy 5083 sensitized at low temperature, Corrosion 72 (2016) 221–241, https://doi.org/10.5006/1766.
[7] W.J. Golumbfskie, K.T. Tran, J.M. Noland, R. Park, D.J. Stiles, G. Grogan, C. Wong, Survey of detection, mitigation, and repair technologies to address problems caused by sensitization of Al-Mg alloys on navy ships, Corrosion 72 (2016) 314–328, https://doi.org/10.5006/1916.
[8] J.L. Searles, P.I. Gouma, R.G. Buchheit, Stress corrosion cracking of sensitized AA5083 (Al-4.5 Mg-1.0 Mn), Metall. Mater. Trans. A 32 (2001) 2859–2867, https://doi.org/10.4028/www.scientific.net/MSF.396-402.1437.
[9] J. Seong, G.S. Frankel, N. Sridhar, Inhibition of stress corrosion cracking of sensitized AA5083, Corrosion 72 (2016) 284–296, https://doi.org/10.5006/1798.
[10] J. Seong, G.S. Frankel, N. Sridhar, Corrosion inhibition of sensitized and solutionized AA5083, J. Electrochem. Soc. 162 (2015) C449–C456, https://doi.org/10.1149/2.0501509jes.
[11] Y. Sano, M. Obata, T. Kubo, N. Mukai, M. Yoda, K. Masaki, Y. Ochi, Retardation of crack initiation and growth in austenitic stainless steels by laser peening without protective coating, Mater. Sci. Eng. A 417 (2006) 334–340, https://doi.org/10.1016/j.msea.2005.11.017.
[12] P. Peyre, C. Braham, J. Lédion, L. Berthe, R. Fabbro, Corrosion reactivity of laser-peened steel surfaces, J. Mater. Eng. Perform. 9 (2000) 656–662, https://doi.org/10.1361/105994900770345520.
[13] J.T. Wang, Y.K. Zhang, J.F. Chen, J.Y. Zhou, M.Z. Ge, Y.L. Lu, X.L. Li, Effects of laser shock peening on stress corrosion behavior of 7075 aluminum alloy laser welded joints, Mater. Sci. Eng. A 647 (2015) 7–14, https://doi.org/10.1016/j.msea.2015.08.084.
[14] Y. Zhang, J. You, J. Lu, C. Cui, Y. Jiang, X. Ren, Effects of laser shock processing on stress corrosion cracking susceptibility of AZ31B magnesium alloy, Surf. Coat. Technol. 204 (2010) 3947–3953, https://doi.org/10.1016/j.surfcoat.2010.03.015.
[15] Y. Sano, K. Akita, K. Masaki, Y. Ochi, I. Altenberger, B. Scholtes, Laser peening without coating as a surface enhancement technology, J. Laser Micro Nanoeng. 1 (2006) 161–166, https://doi.org/10.2961/jlmn.2006.03.0002.
[16] Y. Sano, K. Masaki, T. Gushi, T. Sano, Improvement in fatigue performance of friction stir welded A6061-T6 aluminum alloy by laser peening without coating, Mater. Des. 36 (2012) 809–814, https://doi.org/10.1016/j.matdes.2011.10.053.
[17] H. Wang, C. Ning, Y. Huang, Z. Cao, X. Chen, W. Zhang, Improvement of abrasion resistance in artificial seawater and corrosion resistance in NaCl solution of 7075 aluminum alloy processed by laser shock peening, Opt. Lasers Eng. 90 (2017) 179–185, https://doi.org/10.1016/j.optlaseng.2016.10.016.
[18] H. Amar, V. Vignal, H. Krawiec, C. Josse, P. Peyre, S.N. da Silva, L.F. Dick, Influence of the microstructure and laser shock processing (LSP) on the corrosion behaviour of the AA2050-T8 aluminium alloy, Corros. Sci. 53 (2011) 3215–3221, https://doi.org/10.1016/j.corsci.2011.05.066.
[19] U. Trdan, J. Grum, Evaluation of corrosion resistance of AA6082-T651 aluminium alloy after laser shock peening by means of cyclic polarisation and ElS methods, Corros. Sci. 59 (2012) 324–333, https://doi.org/10.1016/j.corsci.2012.03.019.
[20] U. Trdan, J. Grum, SEM/EDS characterization of laser shock peening effect on localized corrosion of Al alloy in a near natural chloride environment, Corros. Sci. 82 (2014) 328–338, https://doi.org/10.1016/j.corsci.2014.01.032.

[21] ASTM G67, Standard Test Method for Determining the Suscepti- bility to Intergranular Corrosion of 5XXX Series Aluminum Alloys by Mass Loss After Exposure to Nitric Acid (NAMLT), ASTM International, (1999).
[22] R. Fabbro, P. Peyre, L. Berthe, X. Scherpereel, Physics and applications of laser-shock processing, J. Laser Appl. 10 (1998) 265–279, https://doi.org/10.2351/1.521861.
[23] P. Mason, M. Divoký, K. Ertel, J. Pilař, T. Butcher, M. Hanuš, S. Banerjee, J. Phillips, J. Smith, M. De Vido, Kilowatt average power 100 J-level diode pumped solid state laser, Optica 4 (2017) 438–439, https://doi.org/10.1364/OPTICA.4.000438.
[24] V.S. Smentkowski, Trends in sputtering, Prog. Surf. Sci. 64 (2000) 1–58, https://doi.org/10.1016/S0079-6816(99)00021-0.
[25] R.H. Jones, D.R. Baer, M.J. Danielson, J.S. Vetrano, Role of Mg in the stress corrosion cracking of an Al-Mg alloy, Metall. Mater. Trans. A Phys. Metall. Mater. Sci. 32 (2001) 1699–1711, https://doi.org/10.1007/s11661-001-0148-0.
[26] R. Zhang, M.A. Steiner, S.R. Agnew, S.K. Kairy, C.H.J. Davies, N. Birbilis, Experiment-based modelling of grain boundary β-phase (Mg_2Al_3) evolution during sensitisation of aluminium alloy AA5083, Sci. Rep. 7 (2017) 1–14, https://doi.org/10.1038/s41598-017-03090-4.
[27] J. Seong, F. Yang, F. Scheltens, G.S. Frankel, N. Sridhar, Influence of the altered surface layer on the corrosion of AA5083, J. Electrochem. Soc. 162 (2015) C209–C218, https://doi.org/10.1149/2.0321506jes.
[28] Jr Macdonald, Impedance Spectroscopy: Emphasizing Solid Materials and Systems, John Wiley Sons Inc., New York, NY, USA, 1987.
[29] A. Kocijan, D.K. Merl, M. Jenko, The corrosion behaviour of austenitic and duplex stainless steels in artificial saliva with the addition of fluoride, Corros. Sci. 53 (2011) 776–783, https://doi.org/10.1016/j.corsci.2010.11.010.
[30] H. Shi, E.-H. Han, F. Liu, Corrosion protection of aluminium alloy 2024-T3 in 0.05 M NaCl by cerium cinnamate, Corros. Sci. 53 (2011) 2374–2384, https://doi.org/10.1016/j.corsci.2011.03.012.
[31] J.H. Sui, W. Cai, Formation of diamond-like carbon (DLC) film on the NiTi alloys via plasma immersion ion implantation and deposition (PIIID) for improving corrosion resistance, Appl. Surf. Sci. 253 (2006) 2050–2055.
[32] J.B. Bajat, I. Milošev, Ž. Jovanović, R.M. Jančić-Heinemann, M. Dimitrijević, V. B. Mišković-Stanković, Corrosion protection of aluminium pretreated by vinyltriethoxysilane in sodium chloride solution, Corros. Sci. 52 (2010) 1060–1069.
[33] R.T. Foley, Localized corrosion of aluminum alloys—a review, Corrosion 42 (1986) 277–288.
[34] A. Sharma, J. Song, D. Furfari, S.R. Mannava, V.K. Vasudevan, Remarkable near-surface microstructure of nanoparticles and oxide film in laser shock peened Al-Zn-Mg-Cu alloy, Scr. Mater. 202 (2021), 114012, https://doi.org/10.1016/j.scriptamat.2021.114012.
[35] C.A. Rodopoulos, J.S. Romero, S.A. Curtis, E.R. De los Rios, P. Peyre, Effect of controlled shot peening and laser shock peening on the fatigue performance of 2024-T351 aluminum alloy, J. Mater. Eng. Perform. 12 (2003) 414–419, https://doi.org/10.1361/105994903770342944.
[36] P. Peyre, R. Fabbro, P. Merrien, H.P. Lieurade, Laser shock processing of aluminium alloys. Application to high cycle fatigue behaviour, Mater. Sci. Eng. A 210 (1996) 102–113, https://doi.org/10.1016/0921-5093(95)10084-9.
[37] J.T. Wang, Y.K. Zhang, J.F. Chen, J.Y. Zhou, K.Y. Luo, W.S. Tan, L.Y. Sun, Y.L. Lu, Effect of laser shock peening on the high-temperature fatigue performance of 7075 aluminum alloy, Mater. Sci. Eng. A 704 (2017) 459–468, https://doi.org/10.1016/j.msea.2017.08.050.
[38] M. Pavan, D. Furfari, B. Ahmad, M.A. Gharghouri, M.E. Fitzpatrick, Fatigue crack growth in a laser shock peened residual stress field, Int. J. Fatigue 123 (2019) 157–167, https://doi.org/10.1016/j.ijfatigue.2019.01.020.
[39] M. Pourbaix. Atlas of Electrochemical Equilibria in Aqueous Solution 307, NACE, 1974.
[40] J.Z. Lu, K.Y. Luo, Y.K. Zhang, C.Y. Cui, G.F. Sun, J.Z. Zhou, L. Zhang, J. You, K. M. Chen, J.W. Zhong, Grain refinement of LY2 aluminum alloy induced by ultra-high plastic strain during multiple laser shock processing impacts, Acta Mater. 58 (2010) 3984–3994, https://doi.org/10.1016/j.actamat.2010.03.026.
[41] U. Trdan, M. Skarba, J. Grum, Laser shock peening effect on the dislocation transitions and grain refinement of Al-Mg-Si alloy, Mater. Charact. 97 (2014) 57–68, https://doi.org/10.1016/j.matchar.2014.08.020.
[42] L. Berthe, R. Fabbro, P. Peyre, L. Tollier, E. Bartnicki, Shock waves from a water-confined laser-generated plasma, J. Appl. Phys. 82 (1997) 2826–2832, https://doi.org/10.1063/1.366113.
[43] A. Sollier, L. Berthe, P. Peyre, E. Bartnicki, R. Fabbro, Laser-matterinteraction in laser shock processing, in: Proceedings of theFirst Int. Symp. High-Power Laser Macroprocessing, 4831 (2003), 463. ⟨https://doi.org/10.1117/12.497617⟩.
[44] U. Trdan, J. Grum, Investigation of corrosion behaviour of aluminium alloy subjected to laser shock peening without a protective coating, Adv. Mater. Sci. Eng. 2015 (2015) 1–9, https://doi.org/10.1155/2015/705306.